Catalysis Science & Technology

PAPER

View Article Online
View Journal | View Issue

Cite this: *Catal. Sci. Technol.*, 2016, 6, 4525

Synthesis of urchin-like Fe_3O_4@SiO_2@ZnO/CdS core–shell microspheres for the repeated photocatalytic degradation of rhodamine B under visible light†

Jinghai Yang,*[a] Jian Wang,[abc] Xiuyan Li,*[a] Dandan Wang[abc] and Hang Song[bc]

Received 3rd December 2015,
Accepted 14th February 2016

DOI: 10.1039/c5cy02090e

www.rsc.org/catalysis

Herein, we developed the design and synthesis of urchin-like Fe_3O_4@SiO_2@ZnO/CdS core–shell microspheres, in which the multiple functional components were integrated successfully into a single microcomposite. The morphology, composition, and optical and magnetic properties of those core–shell microspheres were characterized by various analytical techniques. Photocatalytic performances were evaluated by the photocatalytic elimination of rhodamine B (RhB) under visible light irradiation. Compared with the Fe_3O_4@SiO_2@ZnO microspheres, the Fe_3O_4@SiO_2@ZnO/CdS microspheres show remarkably enhanced visible light photocatalytic activity, benefiting from the sensitization of CdS, which can extend the visible light absorption and facilitate the separation of photoinduced carriers. The amount of CdS in the core–shell microspheres can be controlled by adjusting the SILAR cycles. The effect of the CdS loading amount on the photocatalytic activity was also investigated and the results indicate that Fe_3O_4@SiO_2@ZnO/CdS with 10.1 wt% CdS exhibits the best photocatalytic ability. Furthermore, it is worth noting that these multifunctional microspheres exhibit excellent magnetic response and high stability. The core–shell photocatalysts can also maintain high photocatalytic activity even after running for five cycles.

1. Introduction

In recent years, the construction of materials with well-designed morphology and multiple functions has attracted tremendous attention.[1,2] Especially in the field of semiconductor-based photocatalysis for water purification, photocatalytic abilities are significantly affected by the cooperation effect of different components.[2–4] The selection of the right photocatalytic materials and taking full advantage of their potential becomes particularly important.

Semiconductor-based photocatalysts such as TiO_2, SnO_2, ZnO, and WO_3 have attracted intense interest owing to their important applications in solving the worldwide environmental pollution.[5–8] Among various semiconductor-based photocatalysts, ZnO, with a direct bandgap of 3.37 eV and an exciton binding energy of 60 meV, has received considerable attention due to its high catalytic activity, low toxicity, low cost, and abundant morphologies, and the quantum efficiency of ZnO powder is also significantly larger than that of TiO_2 powder.[9–17] However, the practical application of ZnO in photocatalysis is still restricted by some disadvantageous issues: the fast recombination rate of photoinduced electron–hole pairs, and its wide bandgap responding only to UV light.[9]

To address the above problems, various strategies have been employed such as metal ion doping, sensitization by noble metal nanoparticles, and combining with smaller band-gap semiconductors.[18–25] Among the above strategies, doping with various metal ions can extend the optical absorption range of photocatalysts according to some research.[26] Unfortunately, the doping component always induces structural defects, which play the role of recombination centers and decrease the photocatalytic efficiency.[27] As an alternative strategy, sensitization by noble metal nanoparticles has became an effective method to extend the spectral responsive range and facilitate charge separation in the materials.[28] But the high costs of noble metals restrict their application in large-scale waste water treatment. One of the viable methods is incorporating small band-gap semiconductors with ZnO.[29–31] Among the small band-gap semiconductors, CdS is an excellent candidate because of its low cost, suitable band

[a] *Key Laboratory of Functional Materials Physics and Chemistry of the Ministry of Education, Jilin Normal University, Siping 136000, PR China.*
E-mail: jhyang1@jlnu.edu.cn, lixiuyan@ jlnu.edu.cn; Fax: +86 434 3294566; Tel: +86 434 3294566
[b] *Changchun Institute of Optics, Fine Mechanics and Physics, Chinese Academy of Sciences, Changchun 130033, PR China*
[c] *University of Chinese Academy of Sciences, Beijing 100049, PR China*

† Electronic supplementary information (ESI) available. See DOI: 10.1039/c5cy02090e

gap (2.4 eV) and band-edge levels that are capable of driving both the reduction and oxidation of water under visible light irradiation.[8,30,32] It not only enhances light harvesting but also reduces the recombination of the photogenerated charges.[30,32,33] To date, there have been many studies that have revealed that ZnO/CdS composites could show remarkably enhanced photostability and photocatalytic activities than either individual component.[30–35]

However, on the basis of practicality, one of the major problems that restrains the application of nano- or micro-sized photocatalysts in waste water treatment is the difficulty to separate these photocatalysts after the purifying reaction, which can possibly cause a new type of pollution.[36,37] Conventional separation methods, including centrifugation and filtration, always lead to serious loss of the catalyst, as well as high energy consumption.[5,37] In addition, centrifugation requires large amounts of energy, which may lead to secondary pollution.[38,39] Photocatalysts fixed on thin films facilitate separation and reuse, but they will remarkably reduce the photocatalytic efficiency because of the significantly decreased active surface area. Therefore, it is still a challenge to design a multi-functional photocatalytic system that is both highly photoactive and cost-effective to recycle.[39] In recent years, incorporating catalysts onto magnetic nano- or microparticles has been employed to settle the above issue, as the catalysts can be removed by an external magnet easily under the premise of maintaining photocatalytic activity.[5,37,39–41] Iron oxides (such as Fe_3O_4 and γ-Fe_2O_3) have long been of interest for use in composite materials because of their non-toxicity and highly sensitive magnetic response.[42,43] For example, Feng *et al.* employed a chemical co-precipitation method and dehydrating method to synthesize Fe_3O_4–ZnO hybrid nanoparticles.[44]

In addition, a silica barrier layer always been introduced to prevent the magnetic cores from oxidation and inhibit the migration of photoinduced carriers from the semiconductor photocatalyst to the magnetic core, which would reduce the photocatalytic efficiency of the photocatalyst. For example, Abramson *et al.* employed sol–gel methods to synthesize γ-Fe_2O_3/SiO_2/TiO_2 nanocomposites.[45] Bian *et al.* used a series of chemical routes to fabricate ZnO–Fe_3O_4@SiO_2 nanocomposites.[46]

In this study, we developed a novel method to synthesize urchin-like magnetic ZnO/CdS integrated microspheres using Fe_3O_4 as the inside cores. An inert interlayer of silica was introduced to connect these functional materials and inhibit the migration of photoinduced carriers from the semiconductor photocatalyst to the magnetic core. The final Fe_3O_4@SiO_2@ZnO/CdS core–shell microstructures showed excellent photocatalytic degradation performance towards RhB under visible light irradiation and could be recycled easily using an external magnetic field.

2. Experiments

2.1. Materials and reagents

All the chemicals used in this experiment were all analytically pure and were used without further treatment. Deionized water (resistivity >18.0 MΩ cm) was used throughout the experiment.

2.2. Synthesis

The entire synthesis process for the Fe_3O_4@SiO_2@ZnO/CdS microspheres is illustrated in Fig. 1 and detailed information for each growth step is present below.

Fe_3O_4: Fe_3O_4 magnetic spheres were fabricated using a modified solvothermal reaction according to a previous study.[47] Briefly, $FeCl_3 \cdot 6H_2O$ (2.777 g) was dissolved in ethylene glycol (60 mL) by stirring to form a clear yellow solution. Sodium acetate (4.629 g) and sodium citrate (0.643 g) were then added under vigorous stirring. Subsequently, the obtained yellow solution was transferred into a teflon-lined stainless-steel autoclave (80 mL capacity) and maintained at 200 °C for 12 h, and then cooled to room temperature. The black products were washed with ethanol and deionized water four times and then dried under vacuum at 60 °C for 6 h. The obtained Fe_3O_4 magnetic spheres were denoted as F in the following.

Fe_3O_4@SiO_2: Fe_3O_4@SiO_2 microspheres could be prepared by a modified Stöber method.[48] Typically, F (1.0 g), synthesized above, was redispersed into a mixture of concentrated ammonia solution (13.4 mL, 25 wt%), ethanol (400.0 mL) and deionized water (100 mL) under sonication and mechanical stirring for 0.5 h. After adding tetraethyl orthosilicate (3.5 mL) dropwise, the mixture was mechanically stirred at room temperature for 4 h. Finally, the Fe_3O_4@SiO_2 microspheres were separated and washed four times with ethanol and deionized water with the assistance of a magnet, and then dried under vacuum at 60 °C for 6 h. The prepared Fe_3O_4@SiO_2 core–shell microstructures were named FS for short.

Fe_3O_4@SiO_2@ZnO: ZnO nanorods on FS microspheres were synthesized by a two-step method according to a

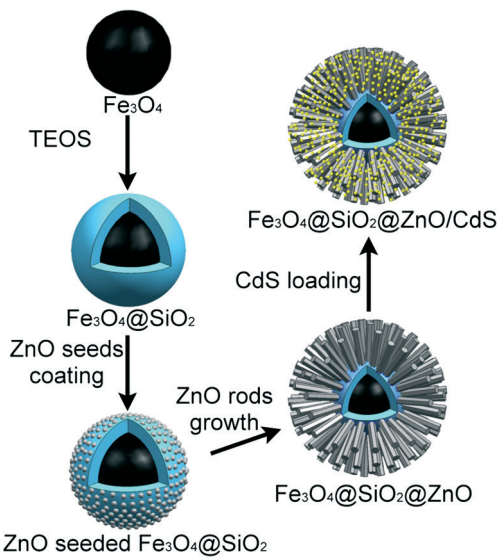

Fig. 1 The synthetic strategy for Fe_3O_4@SiO_2@ZnO/CdS core–shell microspheres.

previous report.[46] (1) Firstly, ZnO nanoparticles were loaded on the surface of the FS microspheres as seeds for the following ZnO nanorods growth, by adding a mixture of ethanol (65 mL) and NaOH (0.3 g) into another solution consisting of ethanol (160 ml), $ZnAc_2{\cdot}2H_2O$ (0.54 g) and the Fe_3O_4@SiO_2 (1.8 g) microspheres. Then, the above reaction system was maintained at 60 °C with mechanical stirring and sonication for 40 min. (2) The seeded FS microspheres, $Zn(NO_3)_2{\cdot}6H_2O$ (1.3 g), and polyvinylpyrrolidone (1.3 g) were added to 200 mL of deionized water and mechanically stirred for 0.5 h to obtain a dispersed solution. Then, a solution consisting of 0.642 g of hexamethylenetetramine in 200 mL of deionized water was added dropwise to the above mixture solution under mechanical stirring. The solution was heated in a microwave oven for 15 min at a power setting of 550 W. (3) Finally, the Fe_3O_4@SiO_2@ZnO microspheres were separated, and washed four times with ethanol and deionized water with the assistance of a magnet, and then vacuum dried at 60 °C for 6 h. The as-synthesized Fe_3O_4@SiO_2@ZnO core–shell microspheres were labeled as FSZ.

Fe_3O_4@SiO_2@ZnO/CdS: CdS nanoparticles were deposited on the surface of the ZnO nanorods through a modified successive ionic layer adsorption and reaction (SILAR) method. Briefly, the samples of FSZ microspheres were successively dipped in two different aqueous solutions for 2 min. One consisted of Cd^{2+} cations (0.1 M $Cd(NO_3)_2$) and the other contained S^{2-} anions (0.1 M Na_2S). Between each immersion step, the samples were washed with deionized water to remove excess ions that were weakly bound to the sample surfaces. The two-step dipping procedure was denoted as one SILAR cycle. Finally, the Fe_3O_4@SiO_2@ZnO/CdS microspheres were separated and washed four times with ethanol and deionized water with the assistance of a magnet, and then vacuum dried at 60 °C for 6 h. The obtained samples in this step were denoted as $FSZC_X$, where X referred to the number of SILAR cycles.

2.3. Characterization

A field emission scanning electron microscope (FESEM, JEOL 7800F) and a transmission electron microscope (TEM, FEI Tenai G^2 F20) were used to characterize the morphologies of all the synthesized samples. Powder X-ray diffraction (XRD) patterns were recorded on a D/max-2500 copper rotating-anode X-ray diffractometer with Cu Kα radiation of wavelength λ = 1.5406 Å (40 kV, 200 mA). The binding energies of the elements in the synthesized samples were performed by X-ray photoelectron spectroscopy (XPS) using a Thermo Scientific ESCALAB 250Xi A1440 system. BET surface areas of the photocatalysts were measured by N_2 adsorption at −196 °C on a nitrogen adsorption apparatus (AUTOSORB-IQ, Quantachrome Instruments, USA). UV-vis diffuse reflectance spectra (DRS) were obtained on a SHIMADZU-UV-3600 spectrophotometer. The photoluminescence (PL) analysis was carried out on a Renishaw inVia micro-PL spectrometer at room temperature (λ_{ex} = 325 nm, He–Cd laser). The magnetic behavior was investigated on a vibrating sample magnetometer (Lake Shore 7407) with an applied field between −14 500 and 14 500 Oe.

2.4. Photocatalysis

RhB was chosen as a model organic pollutant to evaluate the photocatalytic activity of the as-prepared core–shell structured catalysts. Photocatalytic experiments were carried out by using homemade equipment, in which a 250 W Xe lamp equipped with a 420 nm cut-off filter was used to provide the visible light. The distance between the beaker containing the reaction mixture and the light source was fixed at 25 cm. For each photodegradation test, the photocatalyst (60 mg) was added into 60 mL of RhB aqueous solution (7 mg L^{-1}) in a 250 mL beaker. Prior to visible light irradiation, the reaction mixture was mechanically stirred for 15 min in the dark to ensure the adsorption–desorption equilibrium for RhB. Then the reaction mixture was exposed to visible radiation. At a fixed time interval, 3 mL of the suspension was sampled, and magnetically separated to remove the catalyst. Subsequently, the absorbance of RhB solution was recorded using a UV-vis spectrophotometer (UV-5800PC, Shanghai Metash Instruments Co., Ltd) at 555 nm, which is the maximum absorption wavelength of RhB. The progress of photocatalytic degradation of RhB in aqueous solution was calculated using the equation: $C/C_0 = A/A_0$, where C_0 and C are the initial and real-time concentrations of RhB, and A_0 and A represent the initial and real-time absorbances of RhB.

3. Results and discussion

3.1. Characterization of FSZC

At first, to determine the crystallographic structure and phase purity of the samples, the XRD patterns are presented in Fig. 2. All of the characteristic peaks in Fig. 2a can be assigned to the crystal planes of face-centered cubic

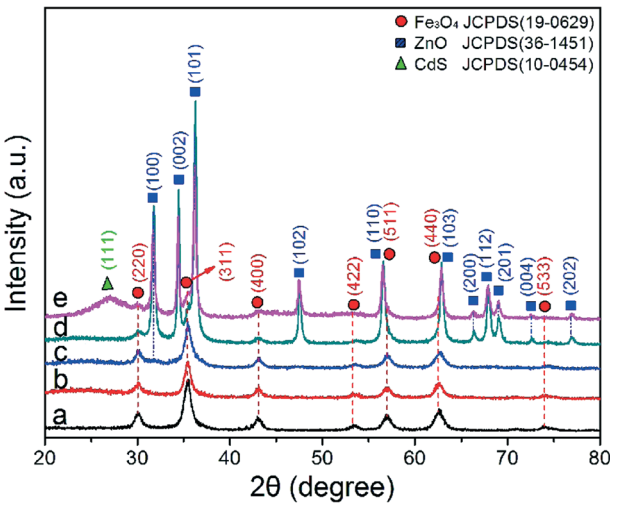

Fig. 2 XRD patterns of the as-prepared samples: (a) F, (b) FS, (c) ZnO seeded FS, (d) FSZ, (e) $FSZC_8$.

structured magnetite Fe_3O_4 (JCPDS no. 19-0629). No impurity peaks are observed. Compared with Fig. 2a, the coating of the SiO_2 layer brings only a small change to the XRD pattern of FS (Fig. 2b). A broad peak detected at about 22° indicates the existence of amorphous SiO_2. After the coating of ZnO seeds on the surface of the FS microspheres, a very tiny peak appears at 31.77° in Fig. 2c, which can be indexed to the (100) crystal plane of hexagonal ZnO (JCPDS no. 36-1451). Obviously, additional diffraction peaks are observed in Fig. 2d after the ZnO rod growth process. Those peaks can also be indexed to the hexagonal ZnO structure. Compared with Fig. 2d, besides the characteristic diffraction of Fe_3O_4 and ZnO, a new diffraction peak at about 27.17° in Fig. 2e can be assigned to the (111) crystal plane of cubic phase CdS (JCPDS no. 10-0454), indicating the successful loading of CdS in the product.

To study the morphologies and structure of the obtained samples, FESEM and TEM measurements were carried out, and the images are presented in Fig. 3 and 4. As shown in Fig. 3a and b, the as-prepared F magnetic cores and FS microspheres exhibit regular spherical shapes, with average diameters of ~390 nm and ~570 nm, respectively. The corresponding TEM image of the F microspheres given in Fig. 4a further supported the FESEM (Fig. 3a) results. Judging from the TEM image of Fig. 4b, after applying a modified Stöber method, the F magnetic cores are coated with a silica shell with an average thickness of ~90 nm. It is observed from Fig. 3c and 4c that the surfaces of the microspheres become rough after the coating of ZnO seeds. After the ZnO nanorod growth process, urchin-like FSZ core–shell microspheres were formed. The ZnO nanorods were uniformly distributed around the surface of the core–shell microstructures, as shown in Fig. 3d. Combined with the TEM image in Fig. 4d, it can be determined that the average length and diameter of the ZnO rods are ~240 nm and ~65 nm, respectively. Finally, CdS nanoparticles were loaded on the multiple-layer microspheres by a SILAR method. It is obvious from Fig. 3e and 4e that small particles are deposited on the surface of ZnO nanorods, making the surfaces of the nanorods much rougher. The HRTEM image of the selected area in Fig. 4e is given in Fig. 4f. There are two different lattice fringes that appear in the HRTEM image. One fringe distance is 0.336 nm, which can be assigned to the lattice fringes of the (111) plane of cubic phase CdS. Another fringe distance is about 0.279 nm, which is indexed to the (110) plane of the hexagonal crystal structure of ZnO. This indicates that a ZnO/CdS heterostructure formed on the surface of the core–shell microspheres.

In order to further confirm the spatial distribution of each element in the as-prepared core–shell microstructures ($FSZC_8$), electron mapping images of a single microsphere are shown in Fig. 5. Obviously different distribution patterns of Fe, Si, Zn, O, Cd and S elements are observed: the Fe signal is located in the center of the microsphere; and gradually surrounded by Si, Zn, O, Cd and S signals. This indicates that the orderly arrangement of the core/shell structure is the

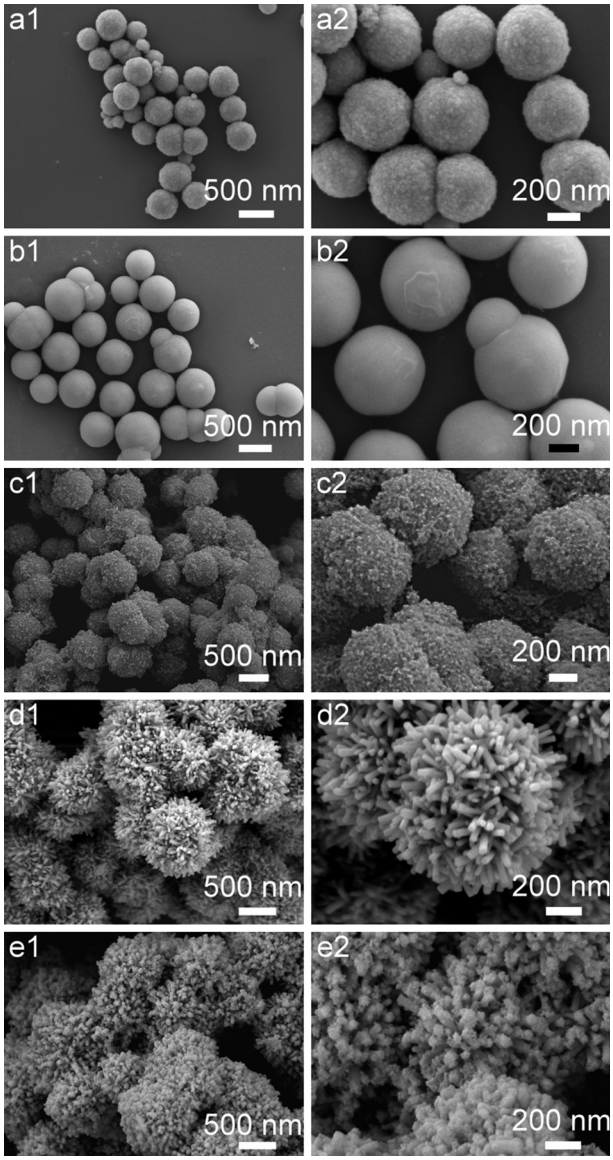

Fig. 3 FESEM images of the as-prepared samples: (a) F, (b) FS, (c) ZnO seeded FS, (d) FSZ, (e) $FSZC_8$.

Fe_3O_4 core, a SiO_2 interlayer, and a ZnO–CdS shell, which confirms the formation of FSZC core–shell microstructures.

In order to study the surface composition and elemental chemical status of the synthesized core–shell samples, FSZ and $FSZC_8$ were investigated by XPS analysis. Fig. 6a shows the fully scanned spectra of the two samples from 0 to 1350 eV. The characteristic peaks on the curve of the FSZ core–shell microspheres in Fig. 6a-I can be indexed to C, Si, Zn, and O elements. After the incorporation of CdS, characteristic peaks for Cd and S can be found on the curve of $FSZC_8$ as shown in Fig. 6a-II. The presence of the C element in both curves depicted in Fig. 6a is mainly attributed to adventitious hydrocarbon contaminants that commonly exist in XPS.[49,50] The peaks of Si 2p, Zn 2p, and O 1s appear in the curves of Fig. 6a-I and Fig. 6a-II, which indicate that FSZ and $FSZC_8$ both contained SiO_2 and ZnO. It is worthy of note that there

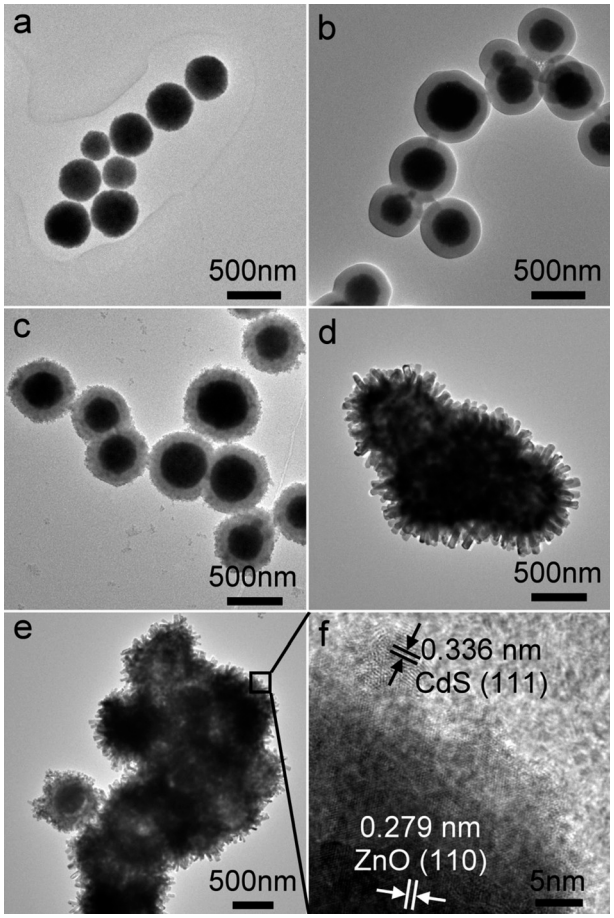

Fig. 4 TEM images of the as-prepared samples: (a) F, (b) FS, (c) ZnO seeded FS, (d) FSZ, (e) $FSZC_8$, (f) HRTEM image for the selected area in (e).

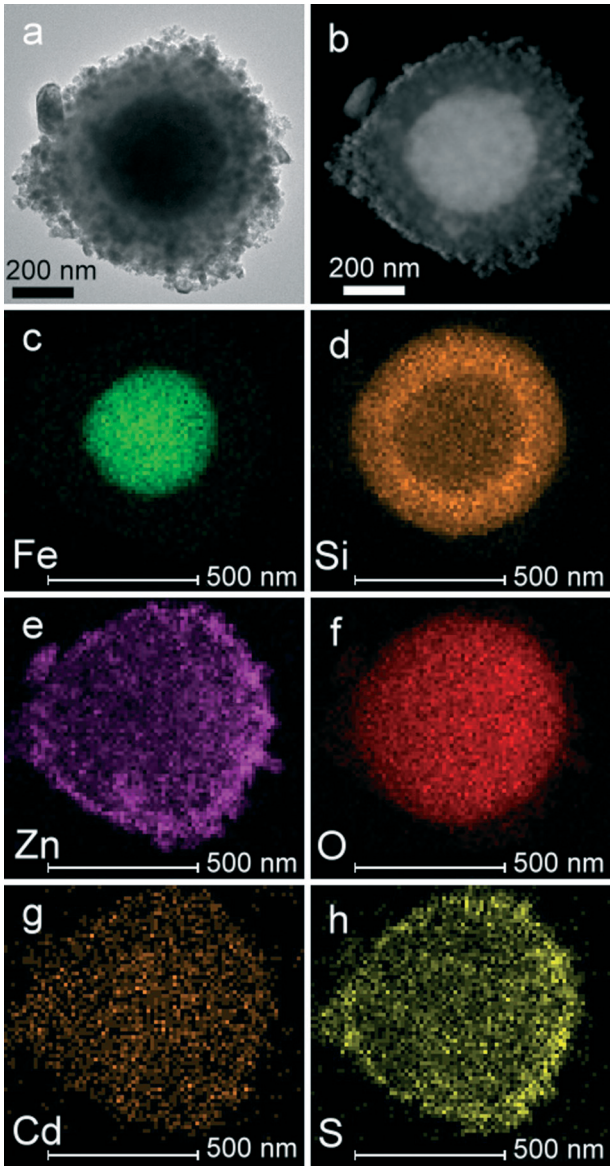

Fig. 5 (a and b) Typical HAADF and TEM image of a single $FSZC_8$ microsphere, (c–h) elemental mapping of a single $FSZC_8$ microsphere from TEM images based on Fe, Si, Zn, O, Cd and S.

is no signal for the Fe element on the curves for both microspheres. That is because XPS is a highly surface-specific technique and the elements can be detected when the depth is less than 10 nm.[49,51] This is powerful evidence to prove that the F cores are tightly wrapped in the center of the microspheres. Based on this fact, it can also be explained why the intensity of the Zn 2p signal is weaker after the loading of CdS nanoparticles on the surface of ZnO, as shown in Fig. 6b. The high resolution XPS spectra of Zn 2p, O 1s, Cd 3d and S 2p are shown in Fig. 6b–e. It can be seen from Fig. 6b that the positions of Zn $2p_{1/2}$ and Zn $2p_{3/2}$ at 1043.7 and 1020.4 eV, with a spin orbit separation of 23.3 eV, indicate that the Zn element existed mainly in the form of Zn^{2+} of ZnO in both core–shell samples.[29,52,53] The O 1s peak in Fig. 6c could be further divided into two different peaks, P_1 and P_2, with binding energies at 531.9 and 530.8 eV, which could be ascribed to the Zn–O in ZnO and hydroxyl groups, respectively.[29,52,53] Furthermore, the high-resolution XPS spectrum of Cd (Fig. 6d) displays the binding energies of Cd $3d_{3/2}$ and Cd $3d_{5/2}$ peaks at 410.4 and 403.8 eV with a splitting energy of 6.6 eV, which are attributed to Cd^{2+} in CdS.[29,51–54] The signal of S in Fig. 6e includes two individual peaks S $2p_{3/2}$ and S $2p_{1/2}$ at 160.2 eV and 161.3 eV with a splitting energy of 0.9 eV, indicating that the valence state of the element S is −2.[29,52–54]

3.2. Characterization of $FSZC_X$

Fig. 7 displays the morphologies of $FSZC_X$ microspheres with increased CdS loading. Obviously, the surface of ZnO rods becomes rougher and rougher because more and more CdS nanoparticles were deposited. Those CdS nanoparticles aggregate together after 10 SILAR cycles. Corresponding XRD patterns of the $FSZC_X$ microspheres with different CdS deposition cycles are shown in Fig. 8 to further confirm the changing of the CdS loading amount on the $FSZC_X$ microspheres. The diffraction peaks of CdS increase with the increase in the number of SILAR cycles, indicating the change

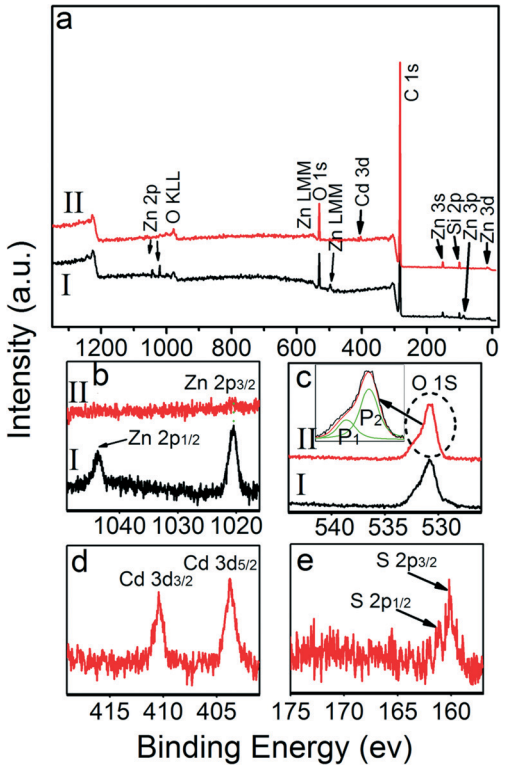

Fig. 6 XPS fully scanned spectra (a) and XPS spectra of Zn 2p (b), O 1s (c), Cd 3d (d), S 2p (e) for FSZ (black lines) and $FSZC_8$ (red lines).

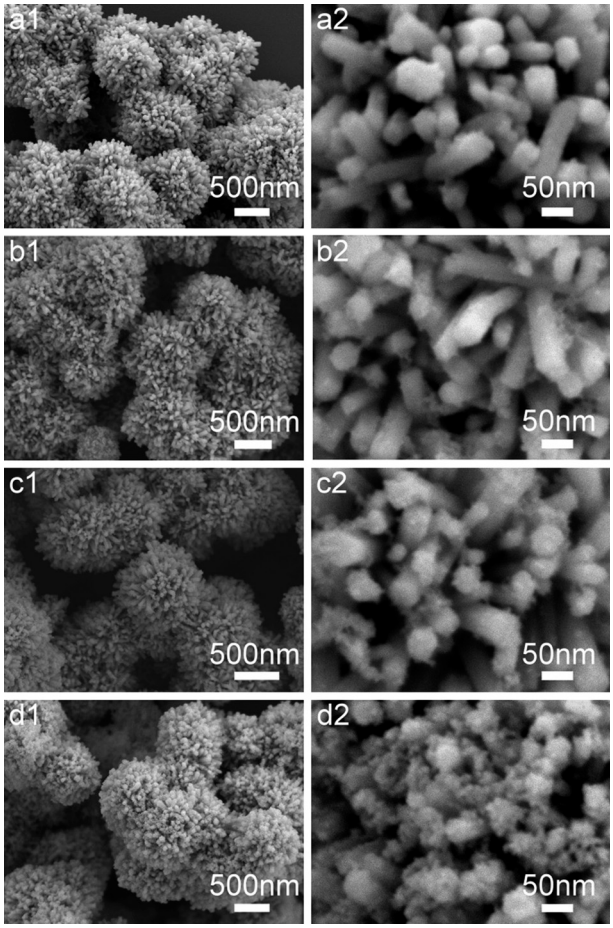

Fig. 7 FESEM images of $FSZC_X$ with different CdS deposition cycles. (a) $FSZC_2$, (b) $FSZC_4$, (c) $FSZC_6$, (d) $FSZC_{10}$.

of the CdS loading amount in the $FSZC_X$ microspheres. Furthermore, as shown in Fig. S1,† EDS analysis was carried out to determine the CdS loading amount in each $FSZC_X$ product. The weight ratio of CdS in the $FSZC_X$ products was calculated and the results are given in Table S1.† The results of the EDS analysis indicate that the CdS loading amount increased from 2.6 wt% to 13.9 wt% when the number of SILAR cycles increased from 2 cycles to 10 cycles.

Nitrogen adsorption–desorption isotherms were recorded to evaluate the effect of the CdS loading amount on the specific surface areas of the $FSZC_X$ products. As shown in Fig. 9, all products show similar type isotherms. The specific surface area of FSZ was calculated using the BET equation and it was found to be 15.57 $m^2\ g^{-1}$. The increase in the CdS loading amount results in variation of the specific surface area as follows: 18.73 $m^2\ g^{-1}$ ($FSZC_2$), 20.07 $m^2\ g^{-1}$ ($FSZC_4$), 21.75 $m^2\ g^{-1}$ ($FSZC_6$), 23.24 $m^2\ g^{-1}$ ($FSZC_8$) and 23.41 $m^2\ g^{-1}$ ($FSZC_{10}$). The specific surface areas of the as-prepared samples increase with the CdS loading amount. Only a slight increase in the specific surface area is observed when the CdS amount increases from 10.1 wt% to 13.9 wt%. This is because the CdS nanoparticles aggregate together when the CdS loading amount is too large.

3.3. Optical properties of the as-prepared microspheres

The light harvesting abilities of the products are related closely to their photocatalytic activities.[30,55] To compare the optical absorption properties of the as-prepared products, UV-vis diffuse reflectance spectra of the as-prepared samples were measured and the results are shown in Fig. 10. The absorption spectrum of FSZ has an absorption edge at about

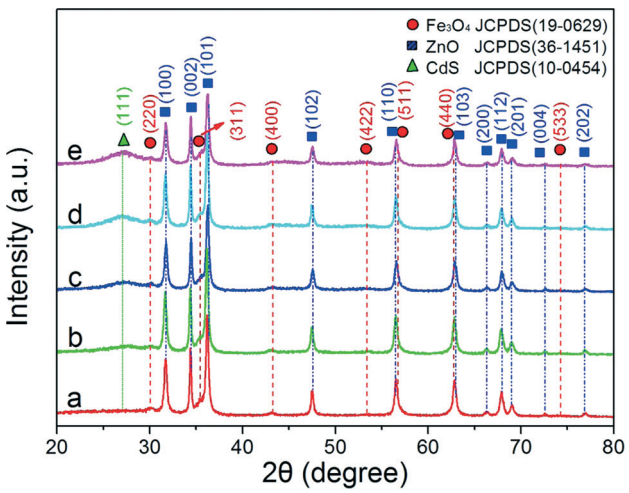

Fig. 8 XRD patterns of $FSZC_X$ microspheres with different CdS deposition cycles. (a) $FSZC_2$, (b) $FSZC_4$, (c) $FSZC_6$, (d) $FSZC_8$, (e) $FSZC_{10}$.

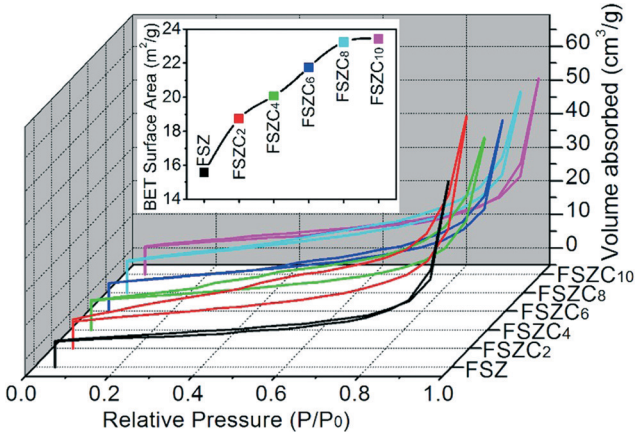

Fig. 9 N_2 sorption isotherms and BET special surface (the inset image) of the as-prepared $FSZC_X$ samples.

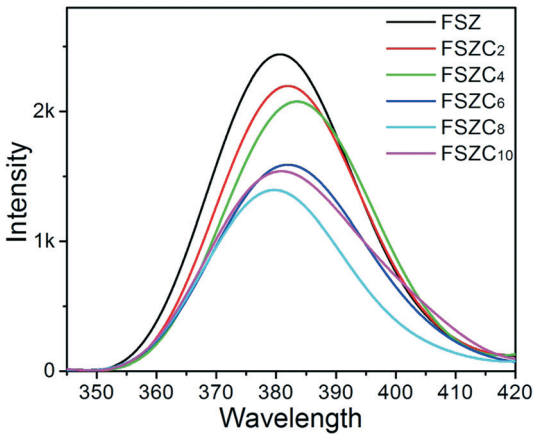

Fig. 11 PL spectra of the as-prepared $FSZC_X$ samples.

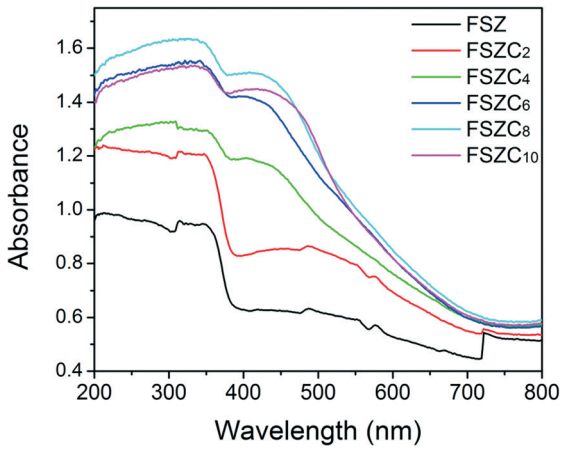

Fig. 10 UV-vis absorption spectra of the as-prepared $FSZC_X$ samples.

400 nm (estimated by the curve tangent) which corresponds to the band-edge absorption of ZnO.[55] In comparison with FSZ, the $FSZC_X$ core–shell microstructures clearly show an added broad and strong absorption in the visible light range. This added absorption from 400 to 550 nm results from CdS loading, which coincides with the literature.[54,56] In addition, the absorption of $FSZC_X$ in the visible region becomes stronger upon increasing the CdS amount in the ZnO surface, by and large. However, the optical absorption decreases when the CdS loading amount increases from 10.1 wt% to 13.9 wt%. This result might be ascribed to the aggregation of CdS on the ZnO surface when the CdS loading amount is too large.[56]

PL emission spectroscopy is able to reflect the efficiency of the charge carrier transfer and trapping of semiconductor photocatalysts due to PL signals arising from the recombination of photogenerated charge carriers.[50,57–59] Therefore, the PL spectra of the as-prepared core–shell products were investigated and the results are shown in Fig. 11. The UV emission centre at about 380 nm can be assigned to the near-band-edge emission of ZnO, and the PL intensity for $FSZC_X$ decreases compared to FSZ.[31] Weaker PL emissions commonly suggest lower recombination rates of photoinduced carriers.[43,60] Firstly, this might result from the loading of CdS nanoparticles reducing the effective area for light absorption of ZnO. Secondly, direct Z-scheme interface photoinduced electron transfer should be responsible for the quenching of PL emission.[9] It can be concluded that the quenching effect is in line with the increment of the CdS loading amount, by and large. However, this trend is not followed for $FSZC_{10}$. The quenching effect shows the order $FSZC_8 > FSZC_{10} > FSZC_6 > FSZC_4 > FSZC_2$. Among all the samples, the intensity of UV emission is the weakest for $FSZC_8$, demonstrating that $FSZC_8$ possesses the most efficient charge separation.

3.4. Photocatalytic properties of the as-prepared microspheres

Photodegradation of RhB under visible light irradiation was chosen as a model reaction to assess the photocatalytic activities of the different samples. The photocatalytic results are plotted in Fig. 12. The photodegradation of RhB without any catalyst was also carried out as a blank test. It is observed from Fig. 12a that in the absence of CdS, FS and FSZ are inert for RhB elimination under visible illumination. After the loading of CdS, the $FSZC_X$ microspheres exhibit obviously enhanced photocatalytic performance. It can be noted that the photocatalytic efficiency of $FSZC_X$ initially increases gradually with the CdS loading amount. However, the photoactivity for $FSZC_X$ decreases upon further increasing the CdS loading amount. The optimum CdS loading amount is 10.1 wt% and $FSZC_8$ shows the highest degradation rate of about 97% at 180 min among all the core–shell microspheres. Hence the photoactivity of all samples determined in the photocatalytic tests follow the order $FSZC_8 > FSZC_{10} > FSZC_6 > FSZC_4 > FSZC_2 > FSZ > FS$. The first order kinetic equation $\ln(C_0/C) = kt$ is also used to fit the experimental data in Fig. 12b, where k is the apparent rate constant. The k value for $FSZC_8$ obtained from Fig. 12b is 0.0213 min^{-1} is the biggest in all core–shell samples, indicating the best photocatalytic activity.

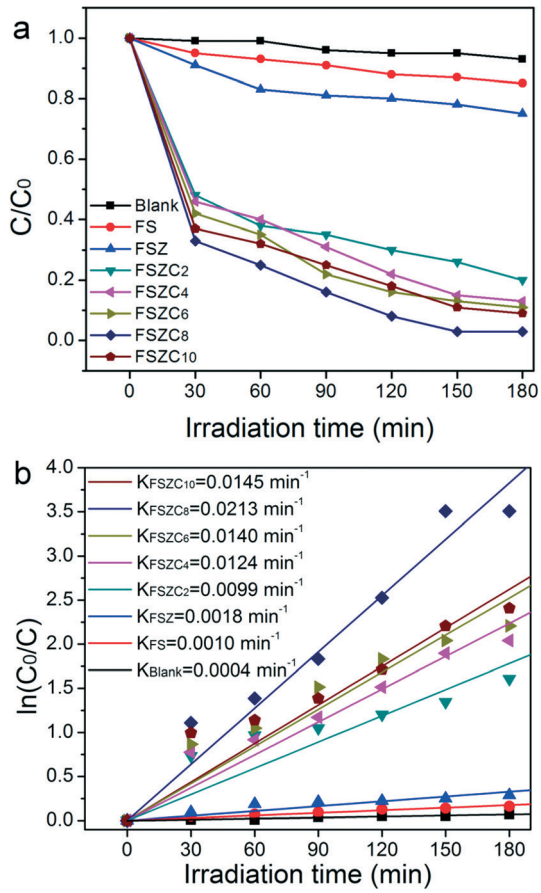

Fig. 12 (a) Photocatalytic decomposition activities during photocatalytic degradation of RhB solutions with various catalysts; (b) the relationship curves of $\ln(C_0/C)$ *versus* reaction time for the different photocatalysts.

Based on the above photocatalytic results, two questions need to be explored in detail. The first question is why all the as-synthesized $FSZC_X$ samples with CdS coatings show enhanced photocatalytic performance compared to FSZ core–shell microspheres. Possible photocatalytic mechanisms are proposed as follows. This can be attributed to the cooperative effect between CdS and ZnO, which is depicted in Fig. 13. Upon visible illumination ($\lambda > 420$ nm), the electrons on the valence band of CdS (VB_{CdS}) can be excited to the conduction band (CB_{CdS}), leaving holes in the VB_{CdS}. These CB_{CdS} electrons migrate into the CB_{ZnO} to reduce the recombination rate of the photogenerated carriers. Then, various photocatalytic active species such as OH and O_2^-, arising from reactions between the photogenerated carriers and OH^- or O_2 or H_2O in the surroundings of the core–shell photocatalysts, concurrently oxidize the organic pollutants to CO_2 and H_2O, thus improving the photocatalytic performances of the core–shell photocatalysts. In addition, the CdS coating lead to a higher BET specific surface, which provides a greater chance for contact between the photocatalyst and the contaminant. The loading of CdS can also expand the absorbance spectrum to the visible range, facilitating the usage of solar light, as revealed by the UV-vis DRS analysis.

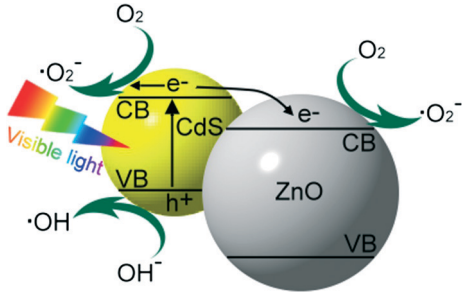

Fig. 13 Schematic energy structure between ZnO and CdS in the $FSZC_X$ composites.

The second question is why $FSZC_8$ shows the best photocatalytic activity among all the as-synthesized $FSZC_X$ samples. The weaker photocatalytic efficiency of the other $FSZC_X$ microspheres can be detailed as follows. When the CdS amount is small, though the dispersion and contact between CdS and ZnO can be better, the amount of photoactive material (here, CdS) is less, and hence the photocatalytic activity will be poor. When overloading too much CdS on the ZnO surface, an aggregation effect can appear. Such aggregation will inhibit the physical contact between CdS and ZnO, that can result in low efficiency for the photoinduced charge transfer to decrease the photocatalytic reaction. This indicates that utilising a proper amount of CdS is an important factor in determining the photocatalytic efficiency.

3.5. Magnetic properties and reusability of samples

To investigate the separation of the as-prepared samples, the magnetic properties was characterized by VSM at 300 K, and field-dependent magnetization curves of F, FS, FSZ and $FSZC_8$ are shown in Fig. 14a. No obvious remanence or coercivity is observed in all the magnetization curve patterns, which indicates that all the samples are superparamagnetic. The magnetization saturation value (M_s) of the Fe_3O_4 core were first measured, and the value is 43.39 emu g^{-1}. After the coating of a SiO_2 interlayer, the M_s value of the FS microspheres decreases to 31.64 emu g^{-1}. Then, after the growth of ZnO nanorods and the loading of CdS nanoparticles, their M_s values are reduced further to 20.63 and 18.97 emu g^{-1}, respectively. However, the final M_s value of the $FSZC_8$ microspheres is sufficiently high for efficient separation and recovery. As shown in the inset image in Fig. 14a, the $FSZC_8$ microspheres can be enriched in 20 s upon the application of an outer magnetic field. Once the magnet was withdrawn, the magnetic particles could be redispersed into the solution again by slightly shaking.

To study the reusability of the $FSZC_X$ core–shell photocatalyst, cycling photocatalytic experiments were carried out over five cycles under visible light, applying a magnet to remove the photocatalysts from solution after each cycle. As shown in Fig. 14b, no obvious decrease in the photocatalytic efficiency of the $FSZC_8$ photocatalyst was observed, even after five circles. In addition, to study the photostability of ZnO,

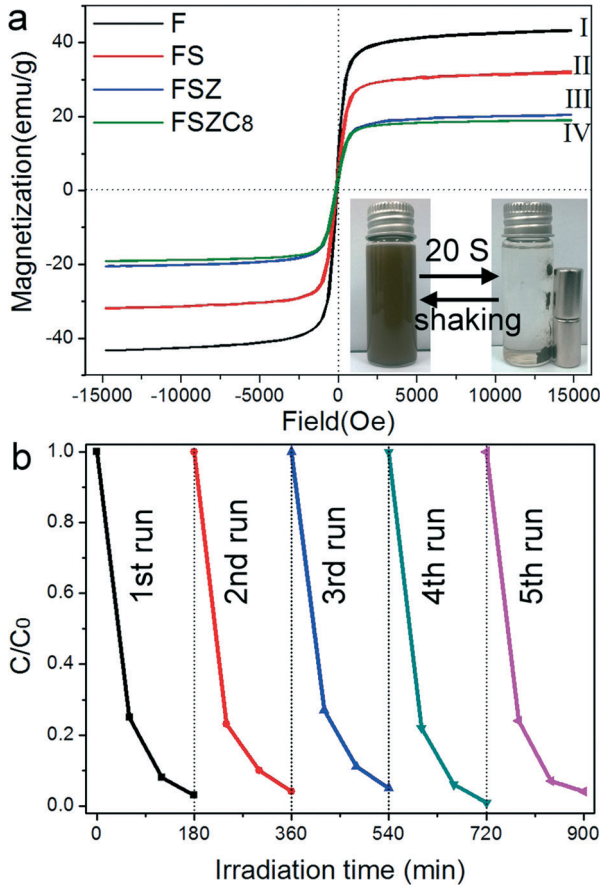

Fig. 14 (a) Magnetic hysteresis loops of the products at room temperature (300 K) (inset image in (a) shows photographs of separation and redispersion processes of the $FSZC_8$ microspheres using a magnet). (b) The reusability of $FSZC_8$ for RhB decoloration.

XRD patterns and SEM images of $FSZC_8$ before and after RhB discoloration are given in Fig. S2.† According to Fig. S2,† there is no obvious change before and after RhB discoloration. This suggests these core–shell $FSZC_X$ microspheres have excellent stability and can serve as reusable photocatalysts for environmental treatment.

4. Conclusions

In summary, urchin-like magnetically retrievable Fe_3O_4@SiO_2@ZnO/CdS (FSZC) core–shell photocatalysts with visible light photocatalytic performance were synthesized successfully. The multilayer structural design contains a highly sensitive magnetic core for convenient magnetic separation, an inert SiO_2 interlayer to protect the Fe_3O_4 core from chemical corrosion and inhibit the migration of photoinduced carriers between ZnO and the Fe_3O_4 core, and a ZnO shell with CdS nanoparticles incorporated on the surface for enhanced photocatalytic activity. The CdS loading amount in the $FSZC_X$ core–shell microspheres can be controlled easily by changing the number of SILAR cycles. Among all the $FSZC_X$ products with different CdS loading amounts, the $FSZC_8$ core–shell photocatalyst can eliminate 97% of RhB in aqueous solution under visible light. The cooperation of CdS and ZnO plays a key role in enabling FSZC to act as a visible light photocatalyst, facilitating the separation of photogenerated carriers. Coating too much or not enough CdS will hinder the electron–hole separation efficiency, and hence decrease the photocatalytic activity. Besides the excellent photocatalytic activity, the easy recyclability and stability of the photocatalysts are other important advantages. Those core–shell photocatalysts can be removed easily by applying a magnet and there is no obvious decrease in the photocatalytic efficiency even after five cycles. Due to their easy magnetic separation, excellent visible light photocatalytic activity for elimination of organic contaminants, as well as their good chemical stability, FSZC core–shell photocatalysts can be potentially applied in practical water purification.

Acknowledgements

This work is supported by the National Programs for High Technology Research and Development of China (863) (item no. 2013AA032202), the National Natural Science Foundation of China (Grant no. 61378085, 51479220 and 61308095), the Program for New Century Excellent Talents in University (no. NCET-13-0824), and the Program for the development of Science and Technology of Jilin province (item no. 20130102004JC, 201215222 and 20140101205JC).

References

1 H. Goesmann and C. Feldmann, *Angew. Chem., Int. Ed.*, 2010, **49**, 1362–1395.
2 Z. Liu, F. T. Chen, Y. P. Gao, Y. Liu, P. F. Fang and S. J. Wang, *J. Mater. Chem. A*, 2013, **1**, 7027–7030.
3 G. Chen, S. Desinan, R. Nechache, R. Rosei, F. Rosei and D. L. Ma, *Chem. Commun.*, 2011, **47**, 6308–6310.
4 Y. H. Deng, Y. Cai, Z. K. Sun, J. Liu, C. Liu, J. Wei, W. Li, C. Liu, Y. Wang and D. Y. Zhao, *J. Am. Chem. Soc.*, 2010, **132**, 8466–8473.
5 C. Y. Li, R. Younesi, Y. L. Cai, Y. H. Zhu, M. G. Ma and J. F. Zhu, *Appl. Catal., B*, 2014, **156–157**, 314–322.
6 L. L. Sun, W. Wu, S. L. Yang, J. Zhou, M. Q. Hong, X. H. Xiao, F. Ren and C. Z. Jiang, *ACS Appl. Mater. Interfaces*, 2014, **6**, 1113–1124.
7 W. He, H. K. Kim, W. G. Wamer, D. Melka, J. H. Callahan and J. J. Yin, *J. Am. Chem. Soc.*, 2014, **136**, 750–757.
8 L. J. Zhang, S. Li, B. K. Liu, D. J. Wang and T. F. Xie, *ACS Catal.*, 2014, **4**, 3724–3729.
9 Z. B. Yu, Y. P. Xie, G. Liu, G. Q. Lu, X. L. Ma and H. M. Cheng, *J. Mater. Chem. A*, 2013, **1**, 2773–2776.
10 B. X. Li and Y. F. Wang, *J. Phys. Chem. C*, 2010, **114**, 890–896.
11 A. Mclaren, T. Valdes-Solis, G. Q. Li and S. C. Tsang, *J. Am. Chem. Soc.*, 2009, **131**, 12540–12541.
12 C. G. Tian, Q. Zhang, A. P. Wu, M. Jiang, Z. Liang, B. Jiang and H. Fu, *Chem. Commun.*, 2012, **48**, 2858–2860.

13 X. Guo, H. J. Zhu and Q. Li, *Appl. Catal., B*, 2014, **160-161**, 408–414.
14 A. B. Djurišić, X. Y. Chen, Y. H. Leung and A. Man Ching Ng, *J. Mater. Chem.*, 2012, **22**, 6526–6535.
15 Z. L. Wang, *Mater. Sci. Eng., R*, 2009, **64**, 33–71.
16 L. H. Yu, W. Chen, D. Z. Li, J. B. Wang, Y. Shao, M. He, P. Wang and X. Z. Zheng, *Appl. Catal., B*, 2015, **164**, 453–461.
17 S. Chakrabarti and B. K. Dutta, *J. Hazard. Mater.*, 2004, **112**, 269–278.
18 M. Mapa and C. S. Gopinath, *Chem. Mater.*, 2009, **21**, 351–359.
19 W. W. Lu, S. Y. Gao and J. J. Wang, *J. Phys. Chem. C*, 2008, **112**, 16792–16800.
20 S. W. Liu, C. Li, J. Yu and Q. J. Xiang, *CrystEngComm*, 2011, **13**, 2533–2541.
21 K. X. Yao, X. Liu, L. Zhao, H. C. Zeng and Y. Han, *Nanoscale*, 2011, **3**, 4195–4200.
22 Y. C. Huang, S. Y. Chang, C. F. Lin and W. J. Tseng, *J. Mater. Chem.*, 2011, **21**, 14056–14061.
23 S. Cho, J. W. Jang, J. Kim, J. S. Lee, W. Choi and K. H. Lee, *Langmuir*, 2011, **27**, 10243–10250.
24 S. M. Jung and K. J. Yong, *Chem. Commun.*, 2011, **47**, 2643–2645.
25 X. Wang, G. Liu, Z. G. Chen, F. Li, L. Wang, G. Q. Lu and H. M. Cheng, *Chem. Commun.*, 2009, 3452–3454.
26 S. Cho, J. W. Jang, J. S. Lee and K. H. Lee, *CrystEngComm*, 2010, **12**, 3929–3935.
27 R. Asahi, T. Morikawa, T. Ohwaki, K. Aoki and Y. Taga, *Science*, 2001, **293**, 269–271.
28 P. Li, Z. Wei, T. Wu, Q. Peng and Y. D. Li, *J. Am. Chem. Soc.*, 2011, **133**, 5660–5663.
29 H. Zhao, Y. M. Dong, P. P. Jiang, G. L. Wang, H. Y. Miao, R. X. Wu, L. G. Kong, J. J. Zhang and C. Zhang, *ACS Sustainable Chem. Eng.*, 2015, **3**, 969–977.
30 F. P. Peng, Q. Zhou, D. P. Zhang, C. H. Lu, Y. Ni, J. H. Kou, J. Wang and Z. Z. Xu, *Appl. Catal., B*, 2015, **165**, 419–427.
31 C. Eley, T. Li, F. L. Liao, S. M. Fairclough, J. M. Smith, G. Smith and S. C. Tsang, *Angew. Chem., Int. Ed.*, 2014, **53**, 7838–7842.
32 X. X. Zou, P. P. Wang, C. G. Li, J. Zhao, D. J. Wang, T. Asefa and G. D. Li, *J. Mater. Chem. A*, 2014, **2**, 4682–4689.
33 X. W. Wang and X. J. Yao, *Carbon*, 2014, **77**, 667–674.
34 J. Fang, L. Xu, Z. Y. Zhang, Y. P. Yuan, S. W. Cao, Z. Wang, L. S. Yin, Y. S. Liao and C. Xue, *ACS Appl. Mater. Interfaces*, 2013, **5**, 8088–8092.
35 S. Liu, M. Q. Yang, Z. R. Tang and Y. J. Xu, *Nanoscale*, 2014, **6**, 7193–7198.
36 X. Guo, N. Chen, C. P. Feng, Y. N. Yang, B. G. Zhang, G. Wang and Z. Y. Zhang, *Catal. Commun.*, 2013, **38**, 26–30.
37 B. Z. Tian, T. T. Wang, R. F. Dong, S. Y. Bao, F. Yang and J. L. Zhang, *Appl. Catal., B*, 2014, **147**, 22–28.
38 V. Belessi, D. Lambropoulou, I. Konstantinou, R. Zboril, J. Tucek, D. Jancik, T. Albanis and D. Petridis, *Appl. Catal., B*, 2009, **87**, 181–189.
39 B. Cui, H. X. Peng, H. Q. Xia, X. H. Guo and H. L. Guo, *Sep. Purif. Technol.*, 2013, **103**, 251–257.
40 X. Xu, X. P. Shen, G. X. Zhu, L. Q. Jing, X. S. Liu and K. M. Chen, *Chem. Eng. J.*, 2012, **200–202**, 521–531.
41 K. Y. Jung and S. B. Park, *Appl. Catal., B*, 2000, **25**, 249–256.
42 W. Wu, X. H. Xiao, S. F. Zhang, F. Ren and C. Z. Jiang, *Nanoscale Res. Lett.*, 2011, **6**, 533.
43 J. Wang, J. H. Yang, X. Y. Li, B. Wei, D. D. Wang, H. Song, H. J. Zhai and X. F. Li, *J. Mol. Catal. A: Chem.*, 2015, **406**, 97–105.
44 X. H. Feng, H. J. Guo, K. Patel, H. Zhou and X. Lou, *Chem. Eng. J.*, 2014, **244**, 327–334.
45 S. Abramson, L. Srithammavanh, J. M. Siaugue, O. Horner, X. Z. Xu and V. Cabuil, *J. Nanopart. Res.*, 2008, **11**, 459–465.
46 X. F. Bian, K. Q. Hong, X. Ge, R. Song, L. Liu and M. X. Xu, *J. Phys. Chem. C*, 2015, **119**, 1700–1705.
47 H. Deng, X. L. Li, Q. Peng, X. Wang, J. P. Chen and Y. D. Li, *Angew. Chem., Int. Ed.*, 2005, **44**, 2782–2785.
48 W. Stöber, A. Fink and E. Bohn, *J. Colloid Interface Sci.*, 1968, **26**, 62–69.
49 Y. Chi, Q. Yuan, Y. J. Li, L. Zhao, N. Li, X. T. Li and W. F. Yan, *J. Hazard. Mater.*, 2013, **262**, 404–411.
50 F. Xu, Y. F. Yuan, H. J. Han, D. P. Wu, Z. Y. Gao and K. Jiang, *CrystEngComm*, 2012, **14**, 3615–3622.
51 Z. Chen and Y. J. Xu, *ACS Appl. Mater. Interfaces*, 2013, **5**, 13353–13363.
52 R. C. Pawar and C. S. Lee, *Appl. Catal., B*, 2014, **144**, 57–65.
53 N. Qin, Y. H. Liu, W. M. Wu, L. J. Shen, X. Chen, Z. H. Li and L. Wu, *Langmuir*, 2015, **31**, 1203–1209.
54 M. Kim, Y. K. Kim, S. K. Lim, S. Kim and S. I. In, *Appl. Catal., B*, 2015, **166–167**, 423–431.
55 Y. J. Wang, F. M. Wang and J. He, *Nanoscale*, 2013, **5**, 11291–11297.
56 J. M. Xu, H. X. Sang, X. T. Wang and K. Wang, *Dalton Trans.*, 2015, **44**, 9528–9537.
57 L. P. Wu, Y. L. Zhang, X. J. Li and C. P. Cen, *Phys. Chem. Chem. Phys.*, 2014, **16**, 15339–15345.
58 L. Q. Jing, H. G. Fu, B. Q. Wang, D. J. Wang, B. F. Xin, S. D. Li and J. Z. Sun, *Appl. Catal., B*, 2006, **62**, 282–291.
59 M. A. Khan, H. T. Jung and O. B. Yang, *J. Phys. Chem. B*, 2006, **110**, 6626–6630.
60 S. A. Ansari, M. M. Khan, M. O. Ansari, J. Lee and M. H. Cho, *J. Phys. Chem. C*, 2013, **117**, 27023–27030.

